Depolarizing Chipless RFID Tag Made Orientation Insensitive by Using Ground Plane Interaction

Zeshan Ali, Olivier Rance, Nicolas Barbot, Etienne Perret

HAL Id: hal-03640641

https://hal.science/hal-03640641

Submitted on 13 Apr 2022

Depolarizing Chipless RFID Tag Made Orientation Insensitive by Using Ground Plane Interaction

Zeshan Ali, Olivier Rance, Nicolas Barbot, and Etienne Perret, *Senior Member, IEEE*

Abstract—**The ground plane has never been considered as a degree of freedom to be used for chipless radio frequency (RF) identification (RFID) tag design purposes. For the first time, we show that the interaction with the ground plane can be exploited to achieve challenging designs like depolarizing tag insensitive to orientation (i.e. non-zero cross polar for any roll angle). The principle relies on the perturbation of the ground plane symmetry with merely one microstrip dipole placed near the edge of the substrate. Chipless RFID tags are realized using three different shapes of the substrate (square, octagonal, and circular) to achieve multiple edges. The measurements are performed in a semi-anechoic and office environment with tag attached to objects (cardboard box and metallic plate). The measured results of the square chipless RFID tags present magnitude variations (<10 dB) but are detectable over a full 360° even in real environment yielding an "orientation insensitive" detection system. Compared to previous designs, the frequency variability of the peaks is negligible.**

Index Terms—**Chipless RFID, cross-polarization, depolarizing, orientation insensitive, radar cross section, scatterer.**

I. INTRODUCTION

CHIPLESS radio frequency (RF) identification (RFID) is potential technology for wireless identification, tracking, environment sensing, and product authentication applications [1]–[3]. The depolarizing chipless RFID tags are one of the fundamental developments of chipless RFID technology for its real-environment practical implementation. The depolarizing nature makes it possible to separate the chipless RFID tags from unwanted signals backscattered by the reflective background objects, thus providing robust reading [4]. However, the depolarizing nature of the chipless RFID tags is primarily

dependent on the orientation which is a significant limitation in practice. In the literature, the orientation independence of cross-polarization chipless RFID is achieved by: 1) the robust reading system and 2) the robust tag design. In [5], a chipless RFID reading system independent of cross-polarization tag orientation is presented. However, the use of two dual-polarized antennas might put constraints on the cost of the system. On the other hand, the design of chipless RFID tags exhibiting both the depolarizing nature and the orientation independence is a very challenging task [6] compared to non-depolarizing designs. Lately, numerous studies have attempted to present the orientation independent depolarizing chipless RFID tags but with limitations such as compactness and radar cross section (RCS) magnitude [6]–[9]. The design principle presented in [7] cannot justify the measurement results as discussed in [8]. The structure of chipless RFID tags is bulky due to the multiple resonators for each resonance frequency. On the other hand, an analytical roll invariance condition for a general scatterer is presented in [6]. In this design, two dipoles exhibiting limited RCS magnitude are used for a resonance frequency, where the length of one dipole is shortened by a few μm compared to the length of another dipole to achieve a phase offset of 90°. Another design exploiting the principle of frequency selective surface (FSS), has been presented in [9]. However, it presents the same kind of limitations as [6] as it needs at least two physical resonators per unit cell for each resonant frequency which makes the design bulky. Also, the resonance frequencies of two sets of dipoles within FSS exhibit a shift of at least 200 MHz, which limits the efficiency in terms of spectral occupancy.

In the literature, the tag orientation insensitivity has also been achieved using co polarization interrogation [10]–[14] and circular polarization interrogation [15]. In co polarization interrogation, the tag orientation insensitivity is mostly based on the rotational symmetric resonators: circular [10], triangular [11], octagonal [12], and trefoil [13]. However, these resonators are non-depolarizing. On the other hand, the co polarization interrogation in [14] can be applied to any chipless RFID tag (non-depolarizing and depolarizing), but this method needs two co polarization measurements.

Circular polarization chipless RFID tag interrogation is discussed in [15] for the purposes of orientation insensitivity while chipless RFID tag is attached to objects (Teflon and metallic platforms) and the clutter removal. A comparison of

circular and cross polarizations chipless RFID tag reading methods is presented in [16]. Based on this comparison, the orientation insensitivity can be achieved using circular polarization interrogation if the measurement environment is semi-anechoic and the ground plane shape is well-chosen. Otherwise, in the real environment, the circular polarization reading is highly impacted by the environment, thus cannot be considered an improvement over the cross polarization reading.

In this paper, we show that exploiting the interaction between the resonators and the ground plane makes it possible to achieve orientation insensitive depolarizing tags using only one microstrip dipole (per peak apex) contrary to [6] or [9]. The ground plane has traditionally been considered only as a metallic screen allowing isolating the tag from the environment but has not been considered as a degree of freedom that can be used for tag design purposes. In this article, we show for the first time that the ground plane interaction can be advantageously used to enhance the tag capabilities. In [6], the objective of the design was to demonstrate the possibility to have truly invariant magnitude under rotation (magnitude deviation less than 2.4 dB) but here, the design is guided by more pragmatic considerations. Efforts are focused on designing a tag that is as easy to read as possible, i.e., a tag with the highest possible RCS for the worst angle. In this context, the term "orientation insensitive" does not mean that the tag's response is angle invariant, but that the RCS remains high enough that the tag is detectable even in a real environment. In addition, the design is focused on achieving the lowest possible frequency deviation and good compactness (single resonator). Furthermore, the proposed circuit design is appropriate for the coding capacity with its compact design and reduced coding channels bandwidth as compared to FSS design in [9] and the high impedance surface (HIS) design in [15].

The organization of this paper is as follows. Section II presents the principle of operation and design parameters. Section III presents the design and realization of the proposed chipless RFID tag. Section IV presents the measurement results. Section V draws conclusions.

II. PRINCIPLE OF OPERATION AND DESIGN PARAMETERS

For all scatterers, the knowledge of the polarization scattering matrix $\mathbf{S} = \begin{bmatrix} S_{vv} & S_{vh} \\ S_{hv} & S_{hh} \end{bmatrix}$ (Sinclair matrix), allows predicting the value of the backscattered field according to the scatterer orientation. It can be shown [6] that the cross-polarization component as a function of orientation $S_{vh}(\theta)$ can be calculated from the knowledge of only two angles, following:

$$S_{vh}(\theta) = S_{vh}(45°) \sin 2\theta + S_{vh}(0°) \cos 2\theta \qquad (1)$$

where the angles are expressed in °. This equation is central to the paper and will be useful both in theory and design.

The design of a classical depolarizing chipless tag consists of a microstrip dipole tilted at 45° (or 135°) and centered on a ground plane [see Fig. 1(a)]. In this case, (1) reduces to $S_{vh}(\theta) = S_{vh}(0°) \cos 2\theta$, so that the component is zero for $\theta =$

45° [90°]. Such a classical depolarizing tag does not feature orientation insensitivity as can be seen in Fig. 1(a).

The condition for orientation invariance for any object and so for depolarizing chipless RFID tag has been derived analytically in [6] and is given by:

$$S_{vh}(45°) = \pm j \, S_{vh}(0°). \qquad (2)$$

By injecting condition (2) in (1), we obtain a circle equation that ensures invariance of $|S_{vh}(\theta)|$. The condition (2) has been fulfilled in [6] using two microstrip dipoles tilted at 0° and 45°, respectively, and slightly shifted in frequency in order to obtain the phase quadrature condition at the operating frequency. The dimensions and the layout of this roll-invariant tag can be seen in [6, Fig. 2] and Fig. 1(b), respectively. The behavior of $S_{vh}(\theta)$ is presented in Fig. 1(b). This design was made to demonstrate strict roll invariance but it has some drawbacks in practice. The operating frequency does not necessarily correspond to the maximum of a peak [see the white dotted line in Fig. 1(b)] and the use of two different resonators results in a wide bandwidth occupation in the vicinity of the operating frequency ($\Delta f = 40$ MHz) [see Fig. 1(b)].
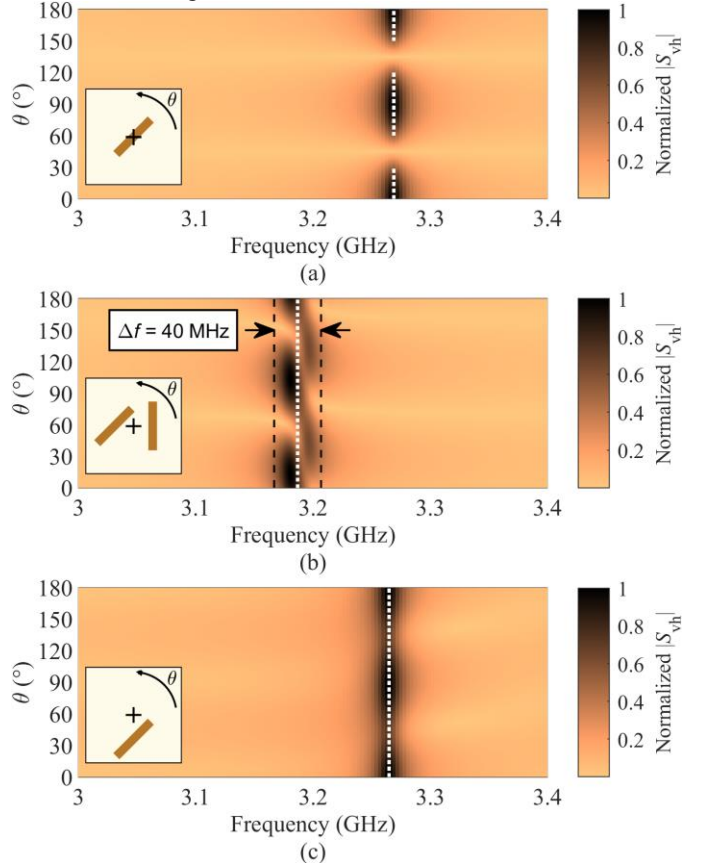

Fig. 1. Evolution of simulated S_{vh} as a function of angle of rotation θ for depolarizing chipless RFID tags. (a) Classical tag design. (b) Roll invariant tag from the literature [6]. (c) Proposed orientation insensitive tag design. CST simulations are used to estimate $S_{vh}(45°)$ and $S_{vh}(0°)$ which are then inserted in (1) to make this plot.

In this paper, the design is driven by practical considerations. Contrary to [6], we do not focus on roll invariance but on roll insensitivity, which means that we aim to maximize the RCS value for the worst case θ. In the general case (1), the trajectory

of $S_{vh}(\theta)$ describes an ellipse in the complex plane, and the quantity to maximize is the semi-minor axis b of the ellipse. Assuming $|S_{vh}(0°)| > |S_{vh}(45°)|$ (which will be the case in the following of the article) the semi-minor axis is given by:

$$b = |S_{vh}(45°)| \cdot \cos\left(\frac{\psi}{2}\right) + |S_{vh}(0°)| \cdot \sin\left(\frac{\psi}{2}\right) \qquad (3)$$

where ψ is defined as a phase error relative to the quadrature condition:

$$\arg\big(S_{vh}(0°)\big) - \arg\big(S_{vh}(45°)\big) = 90° + \psi. \qquad (4)$$

Note that in (3), when the quadrature condition is satisfied ($\psi = 0°$), the problem reduces to maximizing the magnitude of $S_{vh}(45°)$.

In this paper, the maximization of b is fulfilled by using merely one microstrip dipole tilted at 45° (or 135°) and placed near the edge of the ground plane. Using this proposed technique, the microstrip dipole is subjected to ground plane interaction and excited regardless of the orientation of the tag θ as presented in Fig. 1(c). Owing to merely one dipole, the proposed technique utilizes minimal coding channel bandwidth Δf [see Fig. 1(c)] as compared to the techniques presented in [6], [7], [9]. The design details of the proposed tag will be discussed later in this paper.

A. Ground Plane Perturbation

The design principle of the tag will be explained by visualizing the currents induced from an incoming wave on a square ground plane in the presence or absence of a microstrip resonator. In the following, the simulations are performed using a commercial full-wave simulator (CST Microwave Studio). The excitation wave is a linearly polarized plane wave along the y-axis:

$$E(z,t) = E_0 \, e^{jkz - j\omega t + j\phi} \, \hat{y} \qquad (5)$$

where k is wave number, ω is the angular frequency, and ϕ is the initial phase at the reference plane. The x component (cross polarization) of the surface currents is the one of interest and will be referred to as surface currents. The ground plane is a square of side $D = 12$ cm, composed of Rogers RO4003C dielectric with permittivity $\varepsilon_r = 3.55$, and substrate height $h = 0.81$ mm. The microstrip dipole [17] is dimensioned to resonate at $f_r = 3.26$ GHz with its length $L = 24.79$ mm and width $w = 2$ mm. The surface currents are estimated using a field monitor at $f_r = 3.26$ GHz.

The surface currents induced on the ground plane alone are represented in Fig. 2 for two orientations $\theta = 0°$ and $\theta = 45°$. It can be observed that for $\theta = 0°$ the currents are almost null [-60 dB(A/m)]. For $\theta = 45°$ the currents of higher intensity [-45 dB(A/m)] appear on the edges of the structure but are symmetric resulting in a very low cross-polarization component of the E-field in farfield. This result is well known and predicted by the theoretical scattering of perfectly conducting plate $\mathbf{S}^{\text{plate}}$ impinged by a normal incidence plane wave [18]:

$$\mathbf{S}^{\text{plate}} = \frac{4\pi A^2}{\lambda^2} \begin{bmatrix} 1 & 0 \\ 0 & 1 \end{bmatrix} \qquad (6)$$

where A is the area of the metallic plate. It should be noted that any ground plane with n-fold symmetry ($n>2$) will also exhibit a null cross-polarization component [19] in absence of perturbation. This includes the octagon and the circle which will be used later in the article.
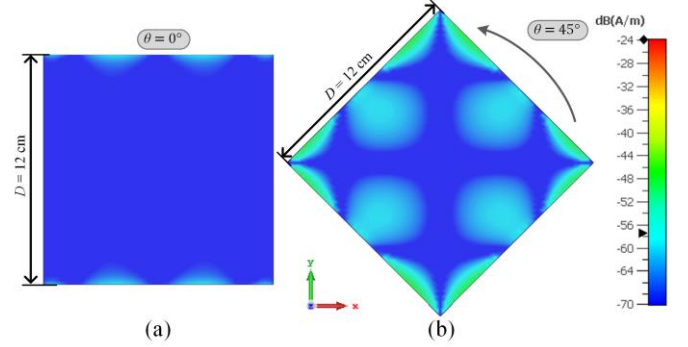

Fig. 2. x components of surface currents of the square dielectric structure backed by a ground plane impinged by a y polarized plane wave. (a) $\theta = 0°$. (b) $\theta = 45°$.

Now we consider the case of the same ground plane but in presence of a microstrip dipole positioned near the edge [with a distance between the center of microstrip dipole and the edge of substrate $R_2 = 1.5$ cm, see Fig. 3(a)] and tilted at an angle $\alpha = 45°$ as represented in Fig. 3. In this configuration, for $\theta = 0°$ and phase excitation $\phi = 0°$ [Fig. 3(a)], the dipole exhibits a maximum backscattered E-field in cross-polarization [maximum surface current around $J_1^{\max} = -24$ dB(A/m)]. On the other hand, the ground plane distribution is symmetrical and does not contribute to the cross-polarization component in the backscattered field.

When the whole scatterer is rotated such that $\theta = 45°$ as shown in Fig. 3(b), the microstrip dipole is aligned with the y polarized incoming wave and presents an insignificant x component (cross polarization) of the surface currents. For this phase excitation $\phi = 0°$, the currents on the edges of the ground plane are exhibiting nulls at the center of the side resulting in a negligible interaction with the dipole

For $\phi = 45°$, the maximum surface current is decreased to around $J_3^{\max} = -33$ dB(A/m) for the scatterer oriented at $\theta = 0°$ [see Fig. 3(c)], but no additional currents appear on the ground plane. On the other hand, for the scatterer oriented at $\theta = 45°$ [see Fig. 3(d)], the current distribution is almost uniform along the edges resulting in non-negligible interaction with the dipole [maximum surface current $J_4^{\max} = -33$ dB(A/m)].

Finally, for $\phi = 90°$, the maximum surface current $J_5^{\max}$ remains equal to $J_3^{\max}$ for the scatterer oriented at $\theta = 0°$ [see Fig. 3(e)]. When the scatterer is oriented at $\theta = 45°$ [see Fig. 3(f)], the currents from the ground plane are concentrated on the center of the edges, resulting in a maximum interaction with the dipole [$J_6^{\max} = -27$ dB(A/m)] and thus completely breaking the symmetry that was observed in Fig. 2.

In this case study we see that: 1) when the structure is oriented at $\theta = 0°$, the backscattered E-field is dominated by the microstrip dipole oriented at 45° such that the ground plane has almost no influence; 2) when the structure is oriented at $\theta = 45°$, the surface current induced on the edges of the ground plane
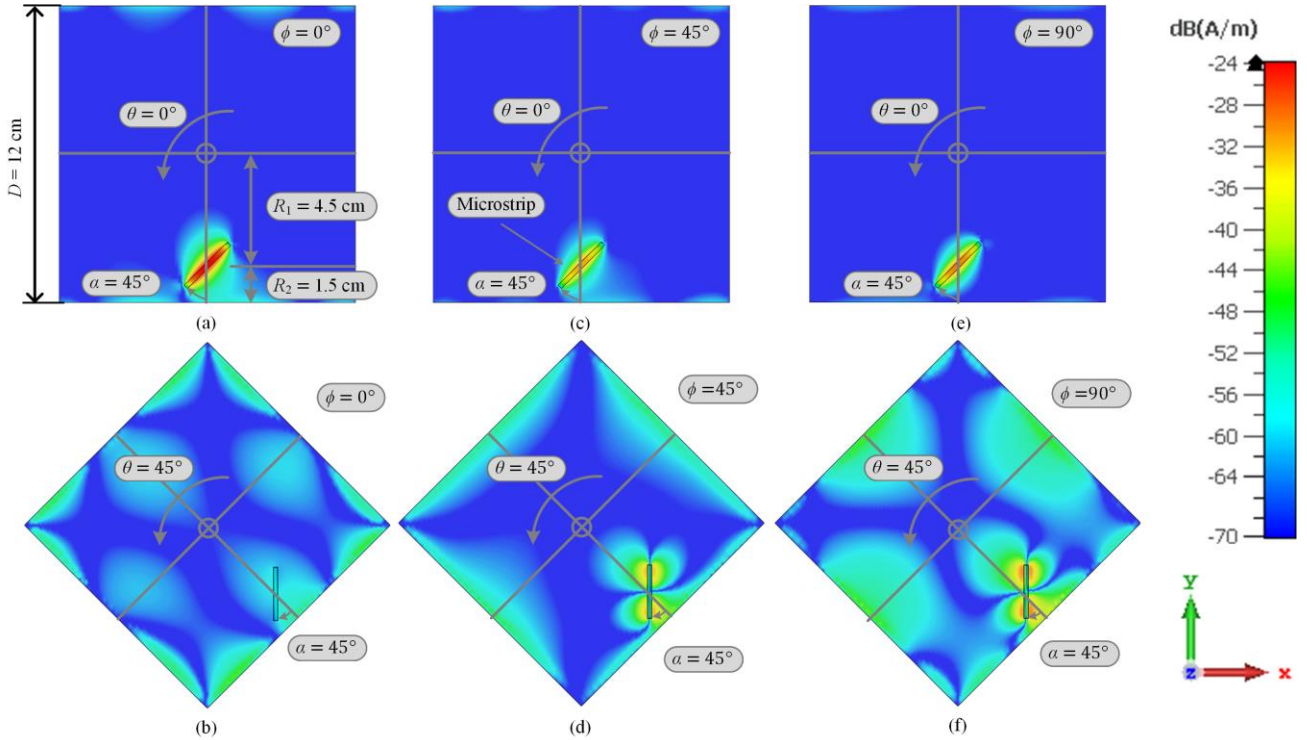
Fig. 3. Principle of ground plane perturbation by showing the x component (cross polarization component) of surface currents for different excitation phase ϕ and the orientation of the scatterer θ for a dipole titled at $\alpha = 45°$. (a) $\theta = 0°$ and $\phi = 0°$. (b) $\theta = 45°$ and $\phi = 0°$. (c) $\theta = 0°$ and $\phi = 45°$. (d) $\theta = 45°$ and $\phi = 45°$. (e) $\theta = 0°$ and $\phi = 90°$. (f) $\theta = 45°$ and $\phi = 90°$. R_1 is the distance from the center of substrate to the center microstrip dipole and R_2 is the distance between the center of microstrip dipole and the edge of substrate. The dipole is placed near the edge of the substrate with $R_1 = 4.5$ cm and $R_2 = 1.5$ cm.

can interact with the microstrip dipole and thus create farfield cross polarization component by breaking the normal symmetry of the ground plane; 3) the surface current for microstrip dipole at $\theta = 0°$ is maximum for $\phi = 0°$, while the interaction between the ground plane and the microstrip $\theta = 45°$ is maximum for $\phi = 90°$ which allows satisfying the quadrature condition (2) for orientation independence.

The backscattered cross polarization E-field (magnitude and phase) of the simulated scatterer (from Fig. 3) oriented at $\theta = 0°$ and $\theta = 45°$ is presented in Fig. 4. For both orientations, the scatterer resonates at $f_r = 3.26$ GHz (exhibiting length $L = 24.79$ mm) with an amplitude difference of 2.96 dB and a phase difference of 93.3° (phase quadrature). These two signals from Fig. 4(a) were utilized in (1) to generate the evolution of the cross-polarization signal S_{vh} in Fig. 1(c). It can be observed that the variation of the resonance frequency f_r is negligible over the range of θ from 0° to 180°.
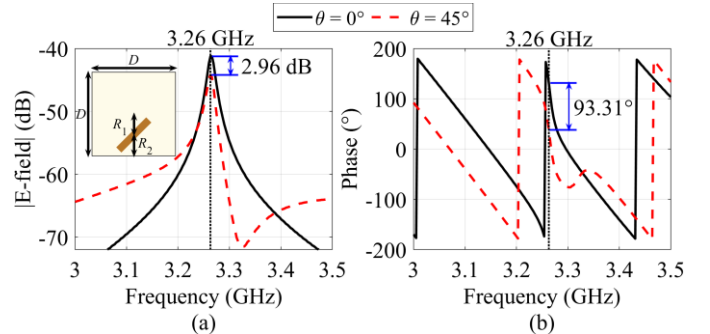

Fig. 4. Simulation of the backscattered E-field of the scatterer oriented at $\theta = 0°$ and $\theta = 45°$. (a) Magnitude. (b) Phase. $D = 12$ cm, $R_1 = 4.5$ cm, and $R_2 = 1.5$ cm.

It is clear that the quadrature condition (4) is almost satisfied ($\psi = 3.31°$) and the problem reduces to maximizing the magnitude of $S_{vh}(45°)$ by optimizing the design parameters of the chipless RFID tag.

B. Effect of Dipole to Substrate's Edge Distance

For the proper ground plane perturbation, R_1 (alternatively R_2) needs to be optimized. Fig. 5 shows the evolution of the peak apex amplitude of simulated cross polarization E-field for two rotation angles $\theta = 0°$ and $\theta = 45°$ while varying R_1 from 20 mm to 50 mm on a $D = 12$ cm square substrate. For $\theta = 45°$, the peak apex presents its maximum amplitude at $R_1 = 4.5$ cm. So, the optimum distance between the center of microstrip dipole and the edge of substrate is found $R_2 = 1.5$ cm.
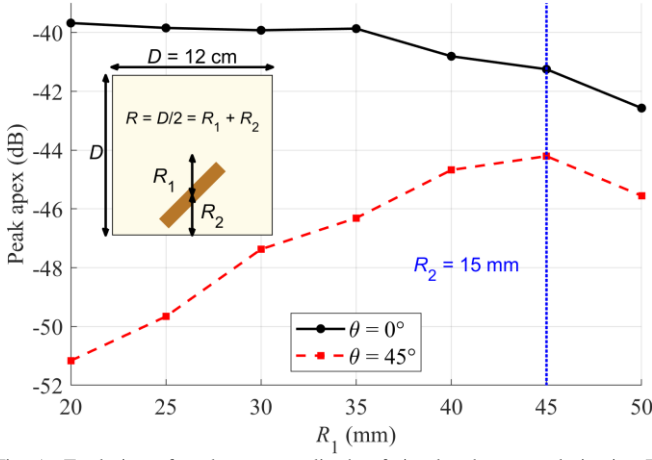
Fig. 5. Evolution of peak apex amplitude of simulated cross polarization E-field as a function of the distance R_1 for two rotation angles $\theta = [0°, 45°]$. Inset: layout of the simulated chipless RFID tag.

C. Effect of Substrate's Size

The substrate's size needs also to be optimized for maximizing the magnitude of $S_{vh}(45°)$ in (3). Fig. 6 shows the evolution of the peak apex amplitude of simulated cross polarization E-field for two rotation angles $\theta = 0°$ and $\theta = 45°$ while changing the side length of square substrate D from 6 cm to 16 cm. For $\theta = 45°$, the peak apex exhibits the maximum amplitude at $D = 12$ cm. But the side length of $D = 12$ cm is quite large for the size of chipless RFID tag. For this reason, the side length of $D = 9$ cm is chosen, which is a trade-off between the size of the tag (similar to the size of the credit card) and its performance.
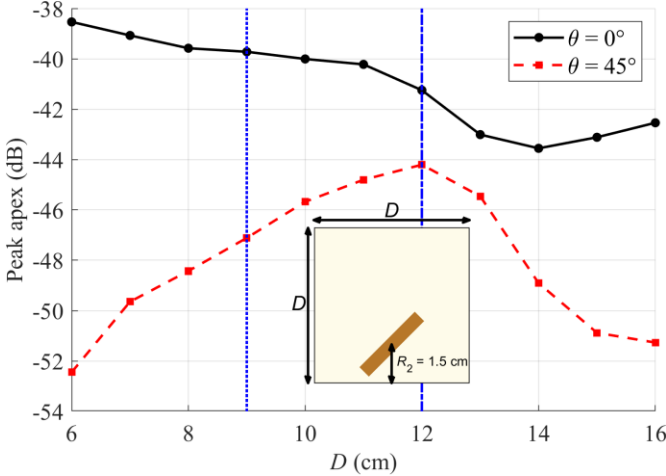

Fig. 6. Evolution of peak apex amplitude of simulated cross polarization E-field as a function of the side length of square substrate D at two rotation angles $\theta = [0°, 45°]$. $R_2 = 1.5$ cm.

D. Effect of Different Shapes of the Substrate

For the proposed technique, the shape of the substrate must exhibit rotational symmetry and multiple edges. Various shapes can be good candidates for this purpose: square, octagonal, and circular. The square can only have four resonators while the octagon can have up to eight, and in the case of the circle, the number of resonators is limited only by their occupation. Here, we have used three shapes of the substrate: square, octagon, and circular [see Fig. 7(inset)]. Fig. 7 shows the evolution of the

peak apex amplitude of simulated cross polarization E-field for two rotation angles $\theta = [0°, 45°]$ with the three aforementioned shapes of the substrate. For $\theta = 45°$, the peak apex of square substrate exhibits the maximum amplitude. So, the square substrate outperforms the octagonal and circular shape, where the circular shape provides the least performance.
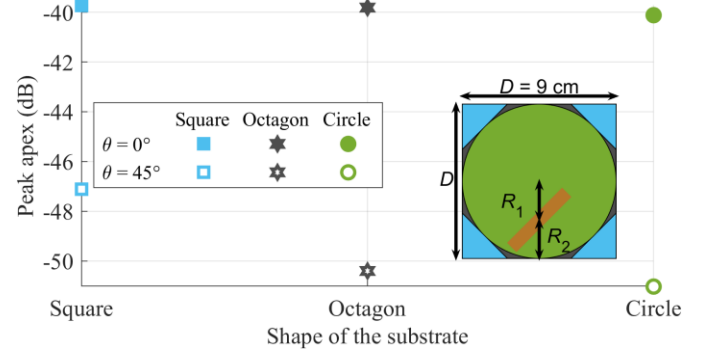

Fig. 7. Evolution of peak apex amplitude of simulated cross polarization E-field as a function of the different shapes of the substrate at two rotation angles $\theta = [0°, 45°]$. Inset: layout of the simulated chipless RFID tag on different shapes of the substrate. R_1=3 cm, R_2=1.5 cm, and D=9 cm.

III. CHIPLESS RFID TAG DESIGN

The tags are fabricated using three shapes of the substrate: square, octagonal, and circular as shown in Fig. 8(a). The dipoles are placed in a circular fashion using polar coordinates: the radius $R_1 = 3$ cm and the angles $\beta_i = [0°, 1·360°/n, 2·360°/n, …]$, where n is the total number of dipoles (i.e., the angles β_i are equally spaced within 360° depending on the number of dipoles). The dipoles are tilted at the inclination angles $\alpha_i = 45°$ or $\alpha_i = 135°$ keeping the distance from the edges $R_2 = 1.5$ cm. The width of the dipole is $w = 5$ mm. The reason behind increasing the value of $w = 5$ mm from the simulated value of $w = 2$ mm (in Figs. 3 to 7) is to increase the RCS. The overall size of the square chipless RFID tags is $D^2 = 9 \times 9$ cm^2. The octagonal and circular chipless tags are sized as inscribed in square chipless tags. So, the diameter of the circular chipless tags is $D = 9$ cm and the length of each side of the octagonal chipless tags is 3.74 cm. The photographs of some realized chipless RFID tags are shown in Fig. 8(b) to (d). The square, octagonal, and circular chipless RFID tags are labeled with the first letter S, O, and C, respectively. The second digit in the labels is 1 (resonators are repeated to improve RCS level) or 2 (all resonators are different). The geometrical dimensions of the realized chipless RFID tags are outlined in Table I. Four chipless RFID tags, namely S2-1, S2-2, S2-3, and S2-4 present the same geometrical dimensions except for the length of the first dipole.
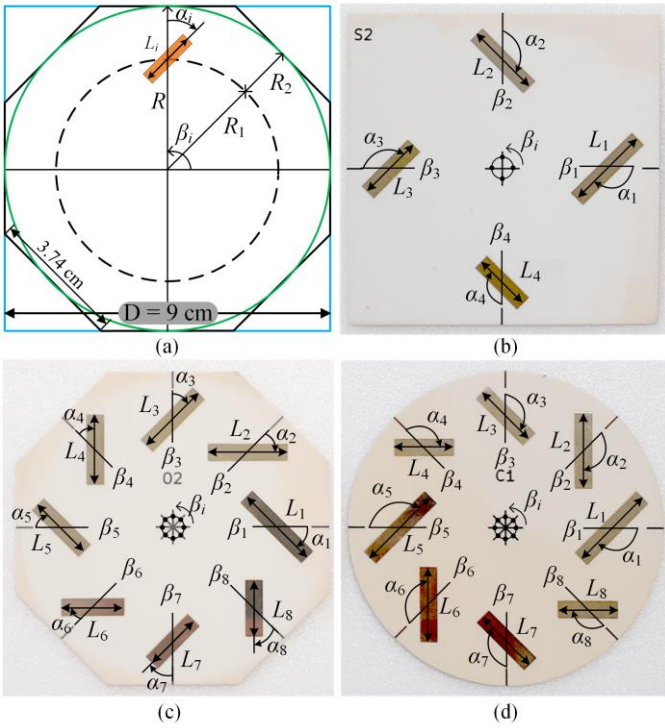
Fig. 8. (a) Illustration of the chipless RFID tags design. Photographs of the realized chipless RFID tags. (b) Square chipless RFID tag. (c) Octagonal chipless RFID tag. (d) Circular chipless RFID tag.

TABLE I
GEOMETRICAL DIMENSIONS OF THE REALIZED SCATTERERS

Scatterers	Length of dipoles L_i (mm)							
	1	2	3	4	5	6	7	8
S1*	24.8	21.5	24.8	21.5				
S1†	24.8	21.5	24.8	21.5				
S2*	24.8	21.5	19.0	17.0				
S2-1†	24.8	21.5	19.0	17.0				
S2-2†	24.1	21.5	19.0	17.0				
S2-3†	23.4	21.5	19.0	17.0				
S2-4†	22.7	21.5	19.0	17.0				
O1‡	24.8	21.5	19.0	17.0	24.8	21.5	19.0	17.0
O2‡	24.8	23.1	21.5	20.2	19.0	18.0	17.0	16.2
C1*	24.8	21.5	19.0	17.0	24.8	21.5	19.0	17.0
C2*	24.8	23.1	21.5	20.2	19.0	18.0	17.0	16.2

* For each ith dipole, α_i is equal to 135°.
† For consecutive pairs of dipoles, α_i and α_{i+1} are equal to 135° and 45°, respectively, where i is an odd number.
‡ For each ith dipole, α_i is equal to 45°.

IV. MEASUREMENT RESULTS

The experimental measurements are done in a semi-anechoic environment using a modified MVG Starlab system as presented in Fig. 9. The monostatic radar setup is configured using one Satimo QH800 dual-polarization horn antenna (0.8 – 12 GHz) and Agilent N5222 vector network analyzer (VNA), where ports 1 and 2 of VNA are connected to V and H ports of antenna, respectively. The output source power of VNA is -5 dBm. The frequency is swept from 2.5 to 5 GHz with 5001

points. Within this frequency sweep range, Satimo QH800 antenna presents the cross-polarization discrimination and port to port isolation larger than 35 dB with a range of gain 8 – 12 dBi [20]. A polystyrene bipod stand is attached to the azimuth motor of the Starlab system to sweep the angle of rotation θ from 0° to 180° with a step size of 5°. The chipless RFID tags are placed on the bipod stand with the antenna to tag distance r = 21.5 cm. The transmission coefficient S_{21} (cross-polarized component) is measured for the entire range of rotation angle $\theta = 0° \leq \theta \leq 180°$. Then, the cross-polarization component S_{vh} of the scattering matrix is calculated using monostatic radar equation [6]

$$S_{vh} = \frac{\left(\sqrt{4\pi}\right)^3 r^2}{G\,\lambda}(S_{21} - S'_{21}) \tag{7}$$

where G is the antenna gain (see [20]) and λ is the free space wavelength, r is the antenna to tag distance, S_{21} is the measured signal in presence of the chipless RFID tag and S'_{21} is the measured signal in absence of the tag (clutter).

A. Square Chipless RFID Tags

The measured cross-polarization signals S_{vh} of S1 chipless RFID tag are presented in Fig. 10. This tag presents two peak apexes because of two dipoles exhibiting the same frequency of resonance (see Table I). The maximum and minimum amplitude values of peak apexes 1 and 2 are -29.55 dB (at θ = 100°) and -40.73 dB (at θ = 145°), and -28.78 dB (at θ = 5°) and -36.71 dB (at θ = 50°), respectively. The variations of magnitude of the peak apexes 1 and 2 are 11.17 dB and 7.93 dB, respectively, for the entire range of rotation angle θ (see Fig. 10). On the other hand, the variations of frequency of resonance of both peak apexes are negligible with a maximum value of 1.8 MHz. Thus, the proposed chipless RFID tag can be read regardless of its orientation which is advantageous as compared to a classical depolarizing chipless RFID tag.
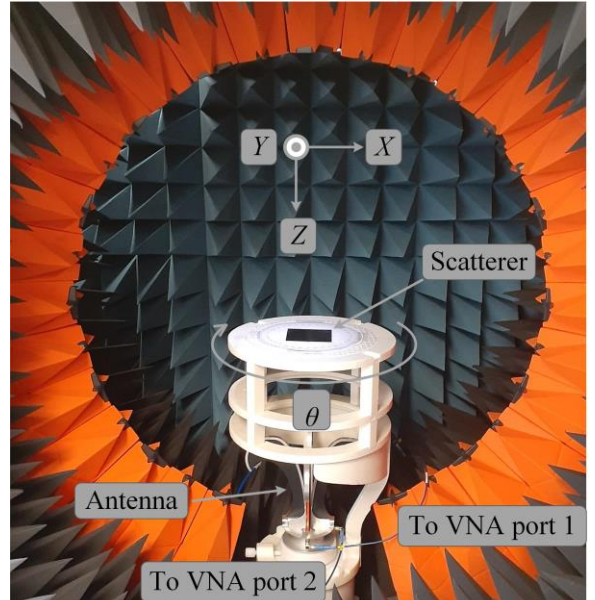

Fig. 9. Photograph of the measurement setup in a semi-anechoic environment.
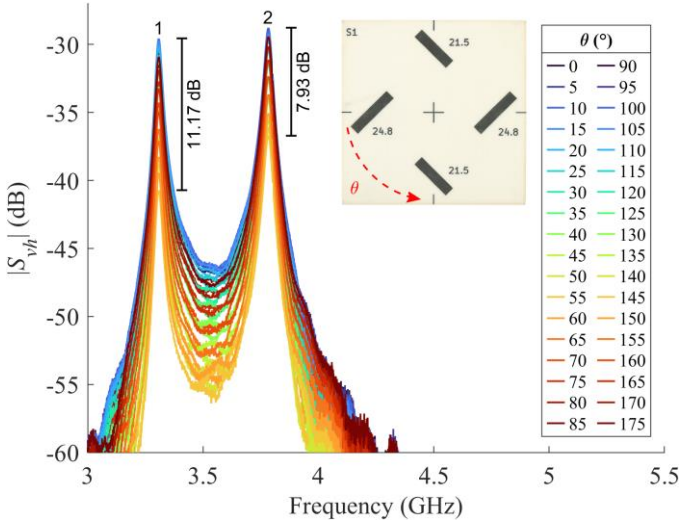
Fig. 10. Measured cross-polarization signals S_{vh} of S1 chipless RFID tag while varying the angle of rotation θ from 0° to 180°. Inset: corresponding photograph of the chipless RFID tag.

The S1′ chipless RFID tag exhibits the same geometrical dimensions as the S1 chipless RFID tag, except for the inclination angles of consecutive dipoles α_i (see Table I). The measured cross-polarization signals S_{vh} of the S1′ chipless RFID tag are presented in Fig. 11. It can be observed that the performance of the S1′ tag (see Fig. 11) is as good as the S1 tag (see Fig. 10) regardless of the inclination angles of consecutive dipoles α_i are set to 135° or 45°. Therefore, in this proposed approach, α_i equal to 45° or 135° can be used.

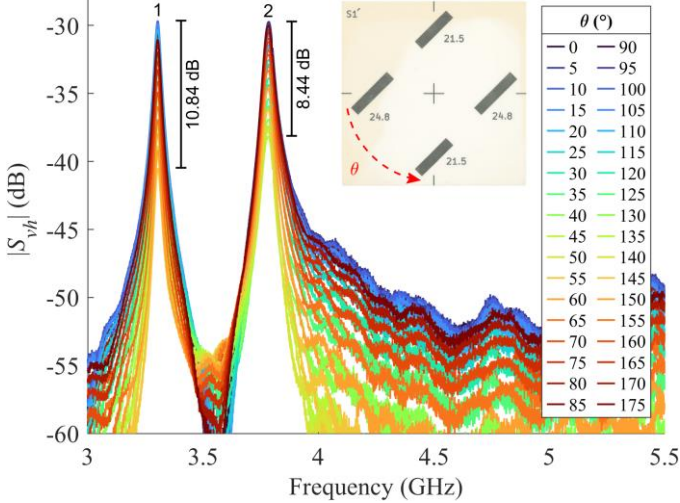Fig. 11. Measured cross-polarization signals S_{vh} of S1′ chipless RFID tag while varying the angle of rotation θ from 0° to 180°. Inset: corresponding photograph of the chipless RFID tag.

Fig. 12 presents the measured cross-polarization signals S_{vh} of the S2 chipless RFID tag. This chipless RFID tag presents four peak apexes because of the different lengths of all four dipoles (see Table I). The maximum and minimum amplitude values of peak apexes 1 to 4 are -35.81 dB (at $\theta = 100°$) and -47.39 dB (at $\theta = 145°$), -35.51 dB (at $\theta = 5°$) and -43.74 dB (at $\theta = 50°$), -34.95 dB (at $\theta = 175°$) and -42.09 dB (at $\theta = 45°$), -35.48 dB (at $\theta = 85°$) and -50.65 dB (at $\theta = 40°$), respectively. The variations of magnitude of the peak apexes 1 to 4 are

11.59 dB, 8.23 dB, 7.14 dB, and 15.18 dB, respectively, for the entire range of rotation angle **θ** (see Fig. 12). The performance of the peak apex 4 is not satisfactory because the minimum value is below -50 dB. The possible reason is that the distance from the edge R_2 has been optimized for 3.26 GHz but should be optimized individually for each resonance frequency. Peak apex 4, gives a good view of the performance degradation that can be expected if the tag is not properly optimized. On the other hand, the variations of frequency of resonance of all the peak apexes are insignificant presenting a maximum value of 3 MHz.

From S2 chipless RFID tag (one dipole for each peak apex) to S1 chipless RFID tag (two dipoles for each peak apex), the average increase in the magnitude of S_{vh} is 6.27 dB. It shows a trade-off between the number of peak apexes and the maximum magnitude of the peak apexes.
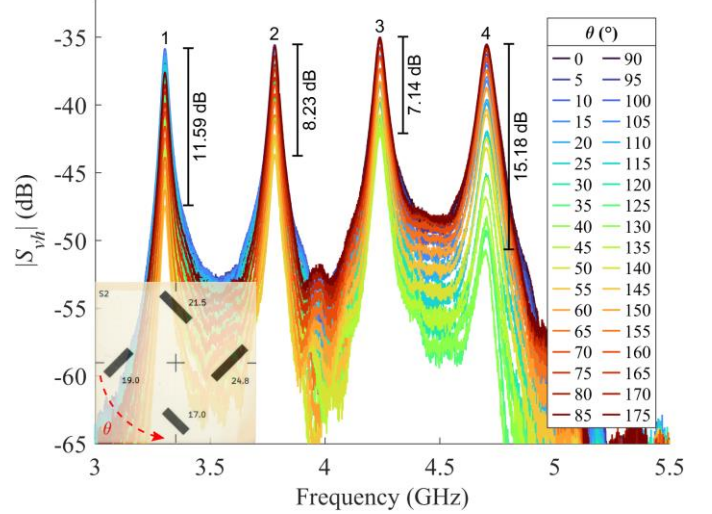

Fig. 12. Measured cross-polarization signals S_{vh} of S2 chipless RFID tag while varying the angle of rotation θ from 0° to 180°. Inset: corresponding photograph of the chipless RFID tag.

The chipless RFID tags, namely S2-1, S2-2, S2-3, and S2-4 present the same geometrical dimensions except for the length of the first dipole (see Table I). Fig. 13 shows the measured cross-polarization signals S_{vh} of chipless RFID tag from S2-1 to S2-4 for two values of the rotation angle $\theta = [0°, 45°]$. Peak apexes of set 1 are associated with the first dipole of all four chipless RFID tags. These peak apexes of set 1 are separated apart by an average value of 92.6 MHz and are well detectable. It is also observed that a variation of the first resonator length does not affect the other resonators' resonance frequency. The absence of couplings between the resonators within the tag is an important advantage in terms of ease of design. Such square chipless RFID tags present very slight variations of frequency of resonance, that is, 3 MHz (see the discussion of Fig. 12). So, the channel coding bandwidth can be further reduced from 92 MHz to an optimal value (for example 50 MHz) to achieve high coding capacity. However, the nonsystematic fabrication process anomalies must be kept in view.

B. Octagonal Chipless RFID Tags

To increase the coding capacity, the octagonal-shaped substrate provides a possibility to have eight dipoles in the

design of chipless RFID tag. The O1 chipless RFID tag has four pairs of dipoles of the same length (see Table I) which leads to four peak apexes in the measurement results of Fig. 14. The maximum and minimum amplitude values of peak apexes 1 to 4 are -29.92 dB (at $\theta = 90°$) and -46.66 dB (at $\theta = 135°$), -29.48 dB (at $\theta = 135°$) and -40.54 dB (at $\theta = 90°$), -29.19 dB (at $\theta = 0°$) and -38.18 dB (at $\theta = 45°$), -27.78 dB (at $\theta = 140°$) and -38.4 dB (at $\theta = 95°$), respectively. The variations of magnitude of the peak apexes 1 to 4 are 16.75 dB, 11.05 dB, 9 dB, and 10.62 dB, respectively, for the entire range of rotation angle θ (see Fig. 14). It can be observed that the O1 chipless RFID tag (see Fig. 14) outperforms the S2 chipless RFID tag (see Fig. 12), as the average increase in the magnitude of S_{vh} is 6.34 dB. Here, too, the variations of frequency of resonance of all four peak apexes are negligible with a maximum value of 3 MHz.
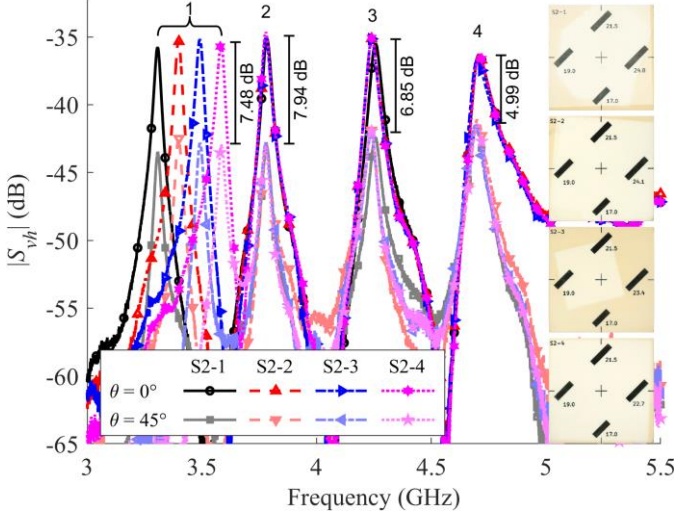

Fig. 13. Measured cross-polarization signals S_{vh} of S2-1, S2-2, S2-3, and S2-4 chipless RFID tags for two values of the angle of rotation $\theta = [0°, 45°]$. Insets: corresponding photographs of the chipless RFID tags.
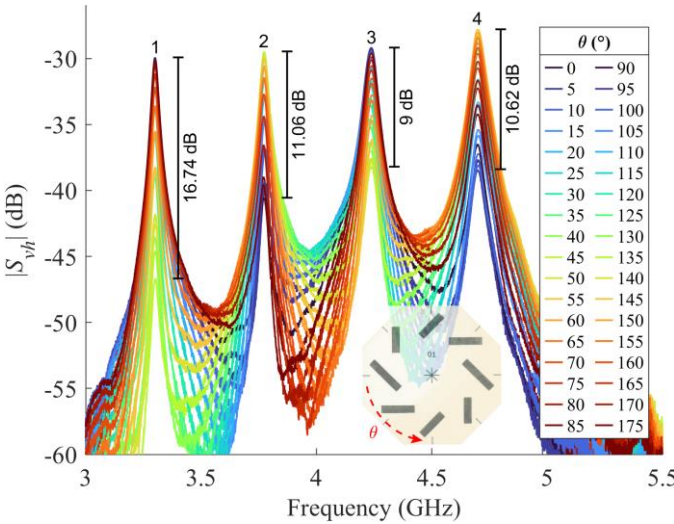

Fig. 14. Measured cross-polarization signals S_{vh} of O1 chipless RFID tag while varying the angle of rotation θ from 0° to 180°. Inset: corresponding photograph of the chipless RFID tag.

The O2 chipless RFID tag exhibits eight dipoles, each with its individual length (see Table I). The measurements present

eight peak apexes as shown in Fig. 15. The performance of this tag is acceptable, except the minimum amplitude of the peak apex 1, that is, -53.84 dB occurring at $\theta = 135°$. On the other hand, the maximum variation of frequency of resonance is presented by the peak apexes, that is, 9.6 MHz.
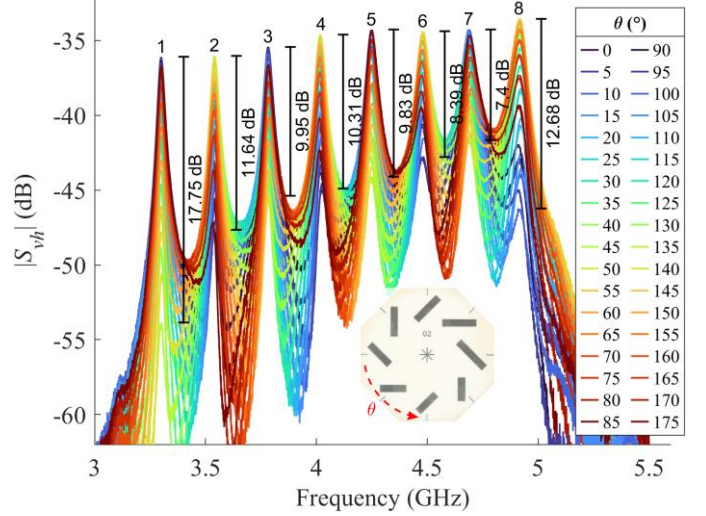

Fig. 15. Measured cross-polarization signals S_{vh} of O2 chipless RFID tag while varying the angle of rotation θ from 0° to 180°. Inset: corresponding photograph of the chipless RFID tag.

C. Circular Chipless RFID Tags

Circular shape substrate has also been studied. The C1 and C2 chipless RFID tags exhibit the same geometrical dimensions as the O1 and O2 chipless RFID tags, respectively, except the shape and the inclination angles α_i. From the measurements, it can be observed that the performance of C1 and C2 chipless RFID tags (Figs. 16 and 17) is inferior to the performance of O1 and O2 chipless RFID tags (Figs. 14 and 15), respectively. The possible reason behind this inferior performance is the curved edge of substrate.
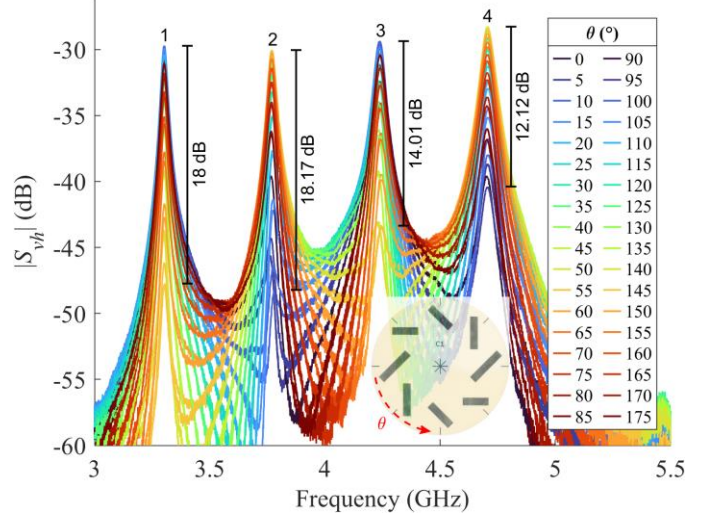

Fig. 16. Measured cross-polarization signals S_{vh} of C1 chipless RFID tag while varying the angle of rotation θ from 0° to 180°. Inset: corresponding photograph of the chipless RFID tag.
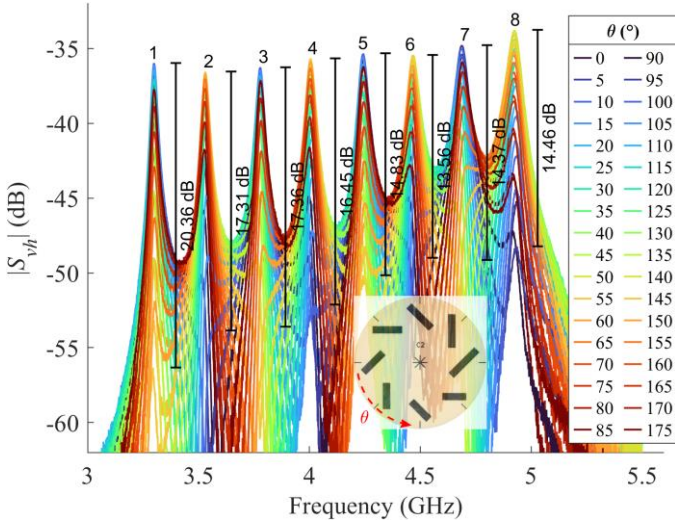
Fig. 17. Measured cross-polarization signals S_{vh} of C2 chipless RFID tag while varying the angle of rotation θ from 0° to 180°. Inset: corresponding photograph of the chipless RFID tag.

D. Performance in Realistic Environment

We have also done the measurement of the chipless RFID tags in a realistic environment (inside an office) as shown in Fig. 18 using essentially the same equipment (VNA-Keysight P9375A, antenna, wires, etc.) and parameters (VNA output power, frequency sweeping, antenna to tag distance r, etc.) as discussed for Fig. 9. Here, the chipless RFID tag is rotated manually from $\theta = 0°$ to $\theta = 180°$ with a step size of 45°.
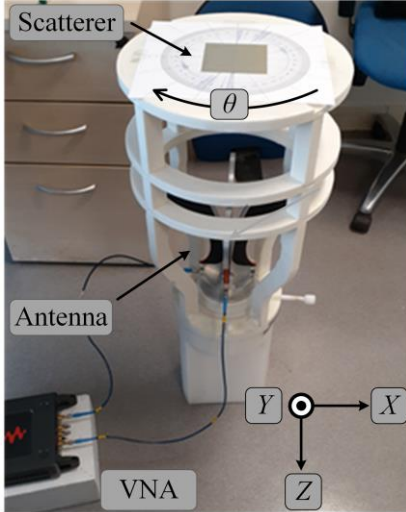

Fig. 18. Photograph of the measurement setup in an office environment.

Three samples of the chipless RFID tags are measured in a realistic environment: S1′ tag (see Fig. 19), S2-1 tag (see Fig. 20), and O1 tag (see Fig. 21). It can be observed that the performance of the S1′, S2-1, and O1 chipless RFID tags in a realistic environment (see Figs. 19, 20, and 21) is comparable to their performance in the semi-anechoic environment (see Figs. 11, 13, and 14). In the cases of S2-1 and O1 tags at $\theta =$ [45°, 135°], the signal-to-noise ratio (SNR) (see Figs. 20 and 21) is reduced; however, their peak apexes are well detectable. Conversely, for the O2 and C2 chipless RFID tags (exhibiting eight peak apexes), we have observed that the SNR is reaching

the detection threshold at $\theta =$ [45°, 135°] in a realistic environment.

Fig. 19. Measured cross-polarization signals S_{vh} of S1′ chipless RFID tag in a realistic environment while varying the angle of rotation θ from 0° to 180°. Inset: corresponding photograph of the chipless RFID tag.

Fig. 20. Measured cross-polarization signals S_{vh} of S2-1 chipless RFID tag in a realistic environment while varying the angle of rotation θ from 0° to 180°. Inset: corresponding photograph of the chipless RFID tag.
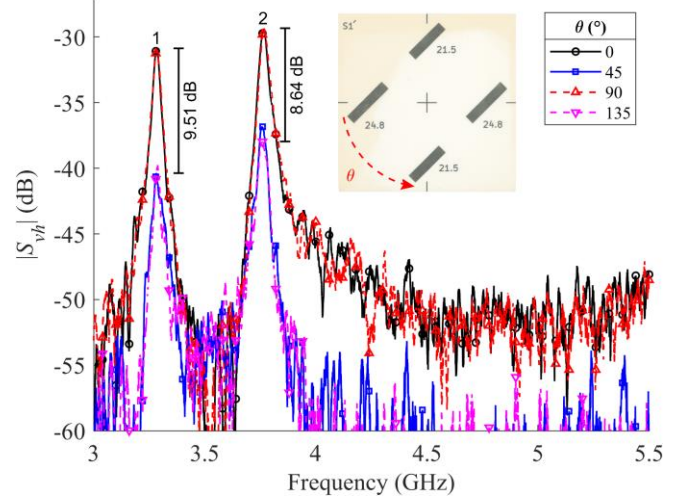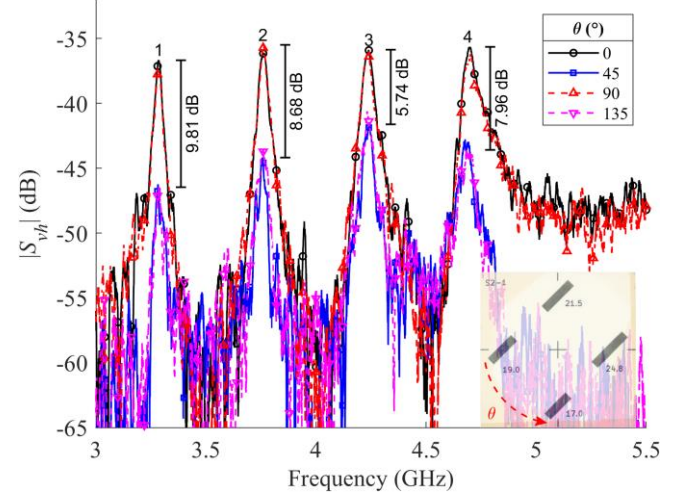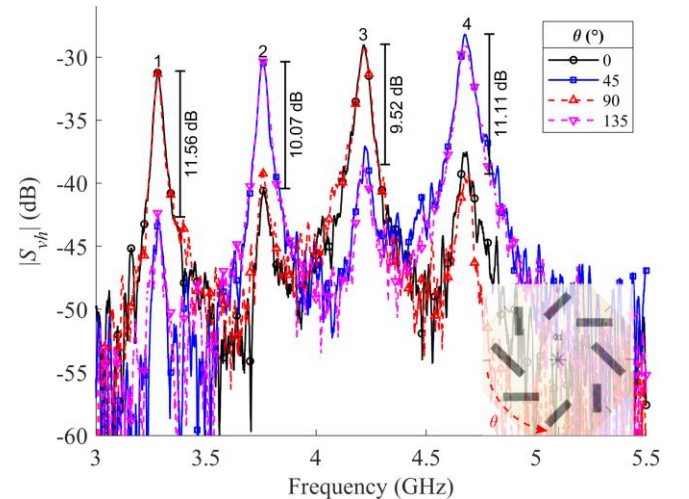

Fig. 21. Measured cross-polarization signals S_{vh} of O1 chipless RFID tag in a realistic environment while varying the angle of rotation θ from 0° to 180°. Inset: corresponding photograph of the chipless RFID tag.

E. Object Contribution in Realistic Environment

Next, the performance of the proposed chipless RFID tag design is characterized when it is attached to the objects: cardboard box (low-scattering) and metallic plate (strong-scattering). The S1 tag is chosen based on its efficient performance (see Figs. 10 or 19). It is important to note that the performance of the S1 tag and the S1′ tag is the same (see the discussion for Fig. 10). The measurements are done in a realistic office environment, where the S1 tag is placed on the Styrofoam spacer and underneath the object. The chipless RFID tag is rotated manually for two values $\theta = 0°$ and $\theta = 45°$.

First, the S1 tag is attached to a cardboard box (with dimensions of $20 \times 15 \times 3.5$ cm^3) keeping the antenna to tag distance $r = 20$ cm as presented in Fig. 22. It can be observed the performance of the S1 tag presents minimal effect while the tag is attached to a cardboard box (see Fig. 22) in comparison to the case of merely the tag (not attached to any object, see Fig. 19).
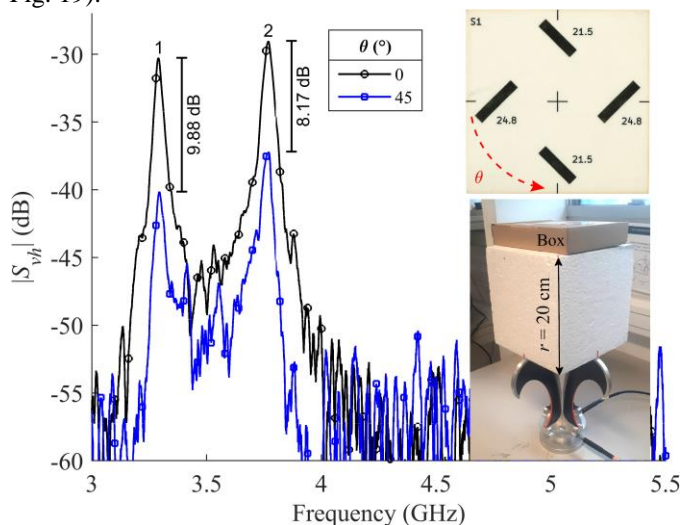

Fig. 22. Measured cross-polarization signals S_{vh} of S1 chipless RFID tag in a realistic environment while the tag is attached to a cardboard box. Insets: photographs of the S1 tag and the measurement setup.

Next, the S1 tag is attached to a metallic plate (with dimensions of 30×20 cm^2). We have observed the proposed chipless RFID tags do not present orientation independence when directly attached to a metallic platform because the highly reflective large metallic platform changes the ground plane symmetry. To avoid such a situation, the metallic plate is separated from the tag by four layers of bubble wrap (i.e., very common in the packaging industry) as presented in Fig. 23. The antenna to tag distance is reduced to $r = 10$ cm to increase the SNR, but the monostatic radar equation (7) might not be valid at $r = 10$ cm (possibly nearfield case). Therefore, Fig. 23 presents the VNA measured calibrated signals $(S_{21} - S'_{21})$. Note that the background signal S'_{21} is measured in the absence of the chipless RFID tag as well as the metallic plate. From Fig. 23, the high reflections (i.e., side peak apexes) from the metallic plate can be observed. Even in such a worst-case, each main peak apex is well detectable because the magnitude difference between the main peak apex and the side peak apex (spurious) is larger than 6.9 dB.

The proposed chipless RFID tags are not dedicated to be read in contact with a metallic plate and it is a limitation compared to classical grounded chipless RFID tags [4]. However, even in the case of classical grounded chipless RFID tags in contact with a metallic plate, the tag reading is challenging and advanced postprocessing techniques are needed, for example, time windowing and short-time Fourier transform (STFT) averaging [21], [22].
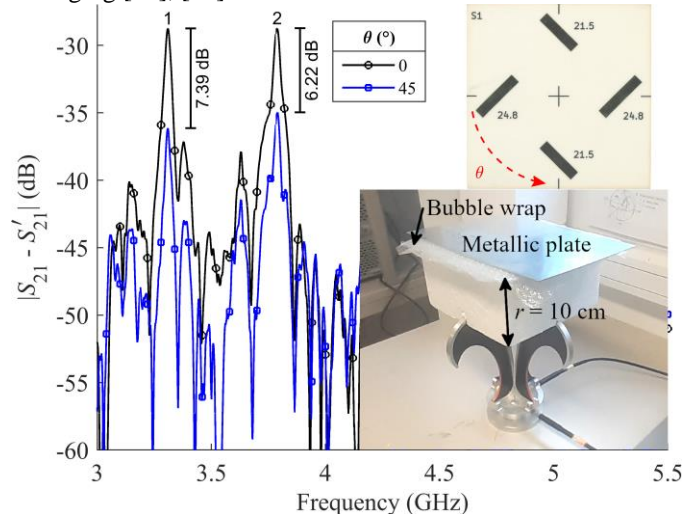

Fig. 23. VNA measured calibrated signals $(S_{21} - S'_{21})$ of S1 chipless RFID tag in a realistic environment while the tag is attached to a metallic plate. Insets: photographs of the S1 tag and the measurement setup.

F. Final Remarks

The proposed chipless RFID tags are frequency coded. It is important to note that the variation of the peak apexes' magnitudes does not affect the decoding of tag code.

The design principle can work for any geometric shape on the condition that the angle between the resonator and the ground plane tangent is 45° (with an observation that the phase quadrature condition is met).

For the future design of the depolarizing chipless RFID tags, attention must be paid while placing the resonator close to the edge of the substrate because ground plane coupling can occur as presented in this paper.

V. CONCLUSION

The possibility to achieve the rotation insensitive cross-polarization chipless RFID tags by using merely one microstrip dipole per coding channel was presented. The proposal was validated by placing the microstrip dipoles near the edge of the substrate to perturb the ground plane (by disturbing the symmetry). Numerous chipless RFID tags with three shapes were realized: square, octagonal and circular. These realized chipless RFID tags were measured in semi-anechoic environment and realistic environment (including while the tag is attached to objects). The proposed chipless RFID tags presented better RCS magnitude than the roll-invariant chipless RFID tags in [6]. Furthermore, the presented chipless RFID tags featured minimal frequency variability of the peak while rotated within an angle range $\theta = 0° \leq \theta \leq 180°$. With such a nominal frequency variability, the coding capacity can be multiple times

by reducing the bandwidth of the coding channel (from 100 MHz as discussed in [4]).

REFERENCES

[1] E. Perret, *Radio Frequency Identification and Sensors: From RFID to Chipless RFID*. Hoboken, NJ, USA: Wiley: Wiley, 2014.

[2] N. C. Karmakar, E. M. Amin, and J. K. Saha, *Chipless RFID Sensors*. Hoboken, NJ, USA: Wiley, 2016.

[3] Z. Ali, E. Perret, N. Barbot, and R. Siragusa, *Chipless RFID Authentication: Design, Realization and Characterization*. London, UK: ISTE Press, to be published.

[4] A. Vena, E. Perret, and S. Tedjni, "A Depolarizing Chipless RFID Tag for Robust Detection and Its FCC Compliant UWB Reading System," *IEEE Trans. Microw. Theory Techn.*, vol. 61, no. 8, pp. 2982–2994, Aug. 2013.

[5] M. Garbati, E. Perret, R. Siragusa, and C. Halopè, "Toward Chipless RFID Reading Systems Independent of Tag Orientation," *IEEE Microw. Wireless Compon. Lett.*, vol. 27, no. 12, pp. 1158–1160, Dec. 2017.

[6] O. Rance, N. Barbot, and E. Perret, "Design of Planar Resonant Scatterer With Roll-Invariant Cross Polarization," *IEEE Trans. Microw. Theory Techn.*, vol. 68, no. 10, pp. 4305–4313, Oct. 2020.

[7] F. Babaeian and N. C. Karmakar, "Development of Cross-Polar Orientation-Insensitive Chipless RFID Tags," *IEEE Trans. Antennas Propag.*, vol. 68, no. 7, pp. 5159–5170, Jul. 2020.

[8] O. Rance, N. Barbot, and E. Perret, "Comments on Development of Cross Polar Orientation Insensitive Chipless RFID Tags," *IEEE Trans. Antennas Propag.*, 2021.

[9] M. Borgese, F. Costa, S. Genovesi, and G. Manara, "Depolarizing Chipless Tags with Polarization Insensitive Capabilities," *Electronics*, vol. 10, no. 4, 2021.

[10] A. Vena, E. Perret, and S. Tedjini, "High-Capacity Chipless RFID Tag Insensitive to the Polarization," *IEEE Trans. Antennas Propag.*, vol. 60, no. 10, pp. 4509–4515, Oct. 2012.

[11] M. A. Islam, Y. Yap, and N. Karmakar, "'Δ' slotted compact printable orientation insensitive chipless RFID tag for long range applications," in *Proc. 9th Int. Conf. Electrical and Computer Engineering (ICECE)*, Dhaka, Bangladesh, 2016, pp. 283–286.

[12] Y. -H. Cho, F. -P. Lai, and Y. -S. Chen, "Novel Topologies of Resonators for Orientation-Insensitive Chipless Radiofrequency Identification Tags," in *Proc. IEEE Asia-Pacific Microw. Conf. (APMC)*, Marina Bay Sands, Singapore, Dec. 2019, pp. 36–38.

[13] N. Tariq *et al.*, "Orientation Independent Chipless RFID Tag Using Novel Trefoil Resonators," *IEEE Access*, vol. 7, pp. 122398–122407, 2019.

[14] N. Barbot, O. Rance, and E. Perret, "Chipless RFID Reading Method Insensitive to Tag Orientation," *IEEE Trans. Antennas Propag.*, pp. 1–1, 2020, doi: 10.1109/TAP.2020.3028187.

[15] S. Genovesi, F. Costa, F. A. Dicandia, M. Borgese, and G. Manara, "Orientation-Insensitive and Normalization-Free Reading Chipless RFID System Based on Circular Polarization Interrogation," *IEEE Trans. Antennas Propag.*, vol. 68, no. 3, pp. 2370–2378, Mar. 2020.

[16] O. Rance, N. Barbot, and E. Perret, "Comparison between Cross-polarization and Circular Polarization Interrogation for Robust Chipless RFID Reading," will be presented at *51th Eur. Microw. Conf. (EuMC)*, London, UK, 2022.

[17] D. M. Pozar, *Microwave Engineering*, 2nd ed. New York, USA: Wiley, 1998.

[18] G. T. Ruck, D. E. Barrick, and W. D. Stuart, *Radar Cross Section Handbook*, vol. 1, 3 vols. Newport Beach, CA, USA: Peninsula Publishing, 2002.

[19] A. Mackay, "Proof of polarisation independence and nonexistence of crosspolar terms for targets presenting n-fold (n>2) rotational symmetry with special reference to frequency-selective surfaces," *Electron. Lett.*, vol. 25, no. 24, pp. 1624–1625, Nov. 1989.

[20] "Datasheet - Open Boundary Quad-Ridge Horns." MVG, 2019. Accessed: Sep. 20, 2021. [Online]. Available: https://www.mvg-world.com/en/products/antennas/measurement-probes-and-feeds/open-boundary-quad-ridge-horns

[21] R. Tavares de Alencar, Z. Ali, N. Barbot, M. Garbati, and E. Perret, "Practical Performance Comparison of 1-D and 2-D Decoding Methods for a Chipless RFID System in a Real Environment," *IEEE J. Radio Freq. Identification*, vol. 4, no. 4, pp. 532–544, Dec. 2020.

[22] Z. Ali, E. Perret, N. Barbot, and R. Siragusa, "Extraction of Aspect-Independent Parameters Using Spectrogram Method for Chipless Frequency-Coded RFID," *IEEE Sensors J.*, vol. 21, no. 5, pp. 6530–6542, 2021.

Zeshan Ali received the M.S. degree in electrical engineering from King Saud University (KSU), Riyadh, Saudi Arabia, and the Ph.D. degree in optical and radio frequency engineering from the Univ. Grenoble Alpes, Grenoble, France, in 2015 and 2019, respectively. From 2011 to 2016, he was a researcher with the Department of Electrical Engineering, KSU, Riyadh, Saudi Arabia, where he was involved in the design and development of multi-band filters, reconfigurable filters and optimization methods. In 2016, he started his research at the Laboratoire de Conception et d'Intégration des Systèmes (LCIS), Grenoble-INP - Institute of Engineering Univ. Grenoble Alpes, Valence, France and focused on the development of chipless RFID systems for product authentication applications. Since 2019, he has been a Post-Doctoral Researcher with the LCIS, Grenoble-INP - Institute of Engineering, Univ. Grenoble Alpes, Valence, France. His current research interests include chipless RFID, polarimetric radar, and RF filters. Dr. Ali was a recipient of the Honorable Mention from the IEEE MTT France chapter for the student paper competition at the IEEE International Microwave Symposium (IMS) held in June 2018 at Philadelphia, PA, USA.

Olivier Rance received the M.Sc. and Ph.D. degrees in electrical engineering from the Institut National Polytechnique de Grenoble, Université Grenoble Alpes, Valence, France, in 2012 and 2017, respectively. He has been a Post-Doctoral Fellow with the Information Processing and Communications Laboratory (LTCI), Télécom Paris, Paris, France from 2017 to 2019 and with the Université Grenoble Alpes, Valence, France, from 2019 to 2020. Since 2021, he is a Research Engineer with Idyllic Technology, Valence, France. His current scientific interests include leaky-wave antennas, chipless RFID, and RF absorbers.

Nicolas Barbot received the M.Sc. degree and Ph.D. degree from the University de Limoges, France in 2010 and 2013 respectively.
His Ph.D. work in Xlim Laboratory, Limoges, France was focused on error-correcting codes for the optical wireless channel. He also realized a post-doctoral work in joint source-channel decoding at L2S Laboratory, in Gif-sur-Yvette, France. Since September 2014, he has been an Assistant Professor at the Université Grenoble Alpes - Grenoble Institute of Technology, in Valence, France.
His scientific background at LCIS Laboratory, Valence, France covers wireless communications systems based on backscattering principle which include classical RFID and chipless RFID.
His research interests include transponders which cannot be described by linear time-invariant systems. This gathers harmonic transponders which are based on the use of a non-linear component (Schottky diode) or linear time-variant transponders which are based on the modification of their response in the time domain. He also places special interests on antenna design and instrumentation based on these phenomena.

Etienne Perret (S'02–M'06–SM'13) received the Eng. Dipl. degree in electrical engineering from the Ecole Nationale Supérieure d'Electronique, d'Electrotechnique, d'Informatique, d'Hydraulique, et des Télécommunications, Toulouse, France, 2002, and the M.Sc. and Ph.D. degrees in electrical engineering from the Toulouse Institute of Technology, Toulouse, in 2002 and 2005, respectively. From 2005 to 2006, he held a post-doctoral position with the Institute of Fundamental Electronics, Orsay, France. In 2006, he was appointed Associate Professor of electrical engineering at Grenoble INP - Institute of Engineering Univ. Grenoble Alpes, France. From 2014 to 2019, he has been a Junior Member with the Institut Universitaire de France, Paris, France, an institution that distinguishes professors for their research excellence,

as evidenced by their international recognition. From 2015 to 2020, he has been an Appointed Member of the French National Council of Universities. He has authored or co-authored more than 200 technical conferences, letters and journal papers, and books and book chapters. He holds several patents. His works have generated more than 3500 citations. His current research interests include wireless communication systems based on the principle of backscatter modulation or backscattering of EM waves especially in the field of RFID and chipless RFID for identification and sensors. His research interests also include electromagnetic modeling of passive devices for millimeter and submillimeter-wave applications, and advanced computer-aided design techniques based on the development of an automated codesign synthesis computational approach. Dr. Perret has been a Technical Program Committee member of the IEEE International Conference on RFID, the IEEE RFID TA; and currently he is a member of the IMS Technical Paper Review Committee. He was a recipient of several awards like the MIT Technology Review's French Innovator's under 35 in 2013, the French Innovative Techniques for the Environment Award in 2013, the SEE/IEEE Leon Brillouin Award for his outstanding achievement in the identification of an object in an unknown environment using a chipless label or tag in 2016, the IEEE MTT-S 2019 Outstanding Young Engineer Award, the Prix Espoir IMT – Académie des sciences in 2020 and the Grand Prix de l'Electronique Général Ferrié in 2021. He was a Keynote Speaker and the Chairman of several international symposiums. Etienne Perret was awarded an ERC Consolidator Grant in 2017 for his project ScattererID.